

MASS-METALLICITY RELATION FOR LOCAL ANALOGS OF HIGH-REDSHIFT GALAXIES: IMPLICATIONS FOR THE EVOLUTION OF THE MASS-METALLICITY RELATIONS

FUYAN BIAN^{1,6}, LISA J. KEWLEY¹, MICHAEL A. DOPITA^{1,2}, GUILLERMO A. BLANC^{3,4,5}

¹Research School of Astronomy & Astrophysics, Mt Stromlo Observatory, Australian National University, Canberra, ACT, 2611, Australia

²Department of Astronomy, King Abdulaziz University, P.O. Box 80203 Jeddah, Saudi Arabia

³Departamento de Astronomia, Universidad de Chile, Camino del Observatorio 1515, Las Condes, Santiago, Chile

⁴Centro de Astrofísica y Tecnologías Afines (CATA), Camino del Observatorio 1515, Las Condes, Santiago, Chile

⁵Visiting Astronomer, Observatories of the Carnegie Institution for Science, 813 Santa Barbara St, Pasadena, CA, 91101, USA

⁶Stromlo Fellow

ABSTRACT

We revisit the evolution of the mass-metallicity relation of low- and high-redshift galaxies by using a sample of local analogs of high-redshift galaxies. These analogs share the same location of the UV-selected star-forming galaxies at $z \sim 2$ on the [O III] λ 5007/H β versus [N II] λ 6584/H α nebular emission-line diagnostic (or BPT) diagram. Their physical properties closely resemble those in $z \sim 2$ UV-selected star-forming galaxies being characterized in particular by high ionization parameters ($\log q \approx 7.9$) and high electron densities ($n_e \approx 100 \text{ cm}^{-3}$). With the full set of well-detected rest-frame optical diagnostic lines, we measure the gas-phase oxygen abundance in the SDSS galaxies and these local analogs using the empirical relations and the photoionization models. We find that the metallicity difference between the SDSS galaxies and our local analogs in the $8.5 < \log(M_*/M_\odot) < 9.0$ stellar mass bin varies from -0.09 to 0.39 dex, depending on strong-line metallicity measurement methods. Due to this discrepancy the evolution of mass-metallicity should be used to compare with the cosmological simulations with caution. We use the [S II]/H α and [O I]/H α BPT diagram to reduce the potential AGN and shock contamination in our local analogs. We find that the AGN/shock influences are negligible on the metallicity estimation.

Keywords: ISM: evolution – galaxies: abundances – galaxies: ISM – galaxies: high-redshift

1. INTRODUCTION

The dependence of chemical abundances on galaxy properties across cosmic time provides insight into the physical mechanisms regulating the formation and evolution of galaxies (e.g., [Finlator & Davé 2008](#); [Lilly et al. 2013](#); [Davé et al. 2012](#); [Ma et al. 2016](#); [Lu et al. 2015](#)). Correlations between stellar masses of galaxies and their gas-phase oxygen abundances are well established in nearby galaxies ([Tremonti et al. 2004](#); [Savaglio et al. 2005](#); [Kewley & Ellison 2008](#); [Andrews & Martini 2013](#); [González Delgado et al. 2014](#)). Heavy elements that are expelled into the interstellar medium (ISM) by supernovae explosions and stellar winds increase the metallicity of galaxies when their stellar mass is built up. Galaxies with higher stellar masses tend to have higher metallicity than lower mass galaxies. A strong evolution of the mass-metallicity relation has been claimed in high-redshift studies ([Erb et al. 2006](#); [Maiolino et al. 2008](#); [Zahid et al. 2013, 2014a](#); [Ly et al. 2014, 2016](#); [Maier et al. 2014](#); [Steidel et al. 2014](#); [Sanders et al.](#)

[2015](#); [Salim et al. 2015](#); [Guo et al. 2016](#)).

These studies typically use strong nebular emission-line ratios to estimate the gas-phase oxygen abundance based on either photoionization models (e.g., [Kewley & Dopita 2002](#)) or empirical calibrations (e.g., [Pettini & Pagel 2004](#), PP04 hereafter). In particular, high-redshift metallicity measurements rely heavily on the PP04 empirical calibrations. PP04 compiled an extensive sample of H II regions in nearby spiral, irregular and blue compact galaxies and fit the relationship between the metallicities mostly from direct temperature (T_e) method¹ and strong emission-line ratios, including the $N2 = \log([N II]\lambda 6584/H\alpha)$ and $O3N2 = \log([O III]\lambda 5007/H\beta)/([N II]\lambda 6584/H\alpha)$ ratios. These two empirical calibrations based on local H II regions have been widely used to estimate the metallicities of high-redshift galaxies (e.g.,

¹ PP04 also used photoionization models to measure the metallicities for a small fraction of high metallicity objects in their sample.

Erb et al. 2006; Hainline et al. 2009; Bian et al. 2010; Steidel et al. 2014; Sanders et al. 2015).

The interstellar medium (ISM) conditions, including the ionization parameter and the ISM pressure, in high-redshift galaxies are quite different from those in low-redshift galaxies (e.g. Kewley et al. 2013a,b; Steidel et al. 2014). The ISM conditions in high-redshift star-forming galaxies are characterized by ~ 0.6 dex higher ionization parameters and an order of magnitude higher ISM pressures/electron densities than their local counterparts (e.g., Kewley et al. 2013a,b, 2015, 2016; Nakajima & Ouchi 2014; Shirazi et al. 2014; Sanders et al. 2016; Dopita et al. 2016; Bian et al. 2016, hereafter B16). This evolution of the ISM conditions raises questions on the applicability of local metallicity calibrations for high redshift galaxies: Are the empirical calibrations based on the local H II regions still valid for high-redshift galaxies considering the dramatic changes of ISM conditions? How would the high ionization parameters and the high ISM pressure in high-redshift galaxies affect the metallicity estimation based on the $N2$ or $O3N2$ diagnostics?

Photoionization models provide important tools to investigate these questions. Photoionization models can be used to establish the relations between metallicity and certain emission line ratios, such as $R23 = ([O II]\lambda 3727 + [O III]\lambda\lambda 4959, 5007)/H\beta$, depending on the ISM conditions. Therefore, the detailed ISM conditions (e.g., ionization parameter, electron density) are required as inputs for photoionization models. It is thus crucial to obtain high signal-to-noise ratio (S/N) rest-frame optical spectra to detect lines, such as the $[O II]\lambda 3727$, $[O III]\lambda 5007$, and $[S II]\lambda\lambda 6717, 6731$ emission lines. However, the spectra of high-redshift galaxies usually suffer from low S/N (< 5) and limited wavelength coverage. It is difficult to measure the ionization parameter and the electron density in a large sample of individual high-redshift galaxies.

In this paper, we use a sample of local analogs of high-redshift galaxies selected based on their locations on the $[O III]\lambda 5007/H\beta$ versus $[N II]\lambda 6584/H\alpha$ “Baldwin, Phillips & Terlevich” (BPT, Baldwin et al. 1981) diagram. These local analogs have about the same properties as high-redshift galaxies, in particular high ionization parameters and high electron densities. Therefore, these analogs provide local laboratories to study the extreme star formation and the ISM conditions in high-redshift galaxies. We use the well-determined physical conditions of ISM in our analogs and photoionization models to study how the metallicities derived from strong line measurements change with the ISM conditions and the implication for the mass-metallicity relation measurements of high-redshift galaxies. The paper is organized as follows. In Section 2, we describe the se-

lection of the local analogs of high-redshift galaxies and the SDSS reference galaxy sample for the further mass-metallicity relation study. In Section 3, we describe the methods of metallicity measurement used in this paper. In Section 4, we study the mass-metallicity relation in the local analogs and the SDSS reference galaxy sample based on the eight metallicity diagnostics. In Section 5, we discuss how AGNs/strong shocks and the photoionization models affect the metallicity measurements in our local analogs and high-redshift galaxies. In Section 6, we summarize the main conclusions of this paper.

Throughout this paper, we adopt following notations for the diagnostic emission line flux ratios:

$$N2 = \log([NII]\lambda 6584/H\alpha)$$

$$O3N2 = \log([OIII]\lambda 5007/H\beta)/[NII]\lambda 6584/H\alpha$$

$$N2O2 = \log([NII]\lambda 6584/[OII]\lambda 3727)$$

$$R23 = ([OII]\lambda 3727 + [OIII]\lambda\lambda 4959, 5007)/H\beta$$

$$O32 = [OIII]\lambda\lambda 4959, 5007/[OII]\lambda 3727$$

The emission line flux ratios in this work are dust-extinction corrected by adopting Cardelli et al. (1989) dust extinction law and assuming case B recombination ($H\alpha/H\beta = 2.86$ for $T_e = 10^4$ K Osterbrock & Ferland 2006).

2. SAMPLE SELECTION

2.1. Local Analogs of High-redshift Galaxies

We use a sample of local analogs of high-redshift galaxies to study the metallicity estimation in high-redshift galaxies. We select local analogs of high-redshift galaxies using the method developed in B16. B16 have demonstrated that the local galaxies selected based on the BPT diagram share the same ISM conditions as star-forming galaxies at $z \sim 2$.

In this study, we select a sample of local analogs of high-redshift galaxy located in the ± 0.04 dex region of the $z \sim 2.3$ star-forming sequence defined by equation 9 in Steidel et al. (2014) on the $[O III]\lambda 5007/H\beta$ versus $[N II]\lambda 6584/H\alpha$ BPT diagram (Figure 1(a))

$$\log([OIII]/H\beta) > \frac{0.67}{\log([NII]/H\alpha) - 0.33} + 1.09, \quad (1)$$

$$\log([OIII]/H\beta) < \frac{0.67}{\log([NII]/H\alpha) - 0.33} + 1.17, \quad (2)$$

and

$$\log([NII]/H\alpha) < -0.5 \quad (3)$$

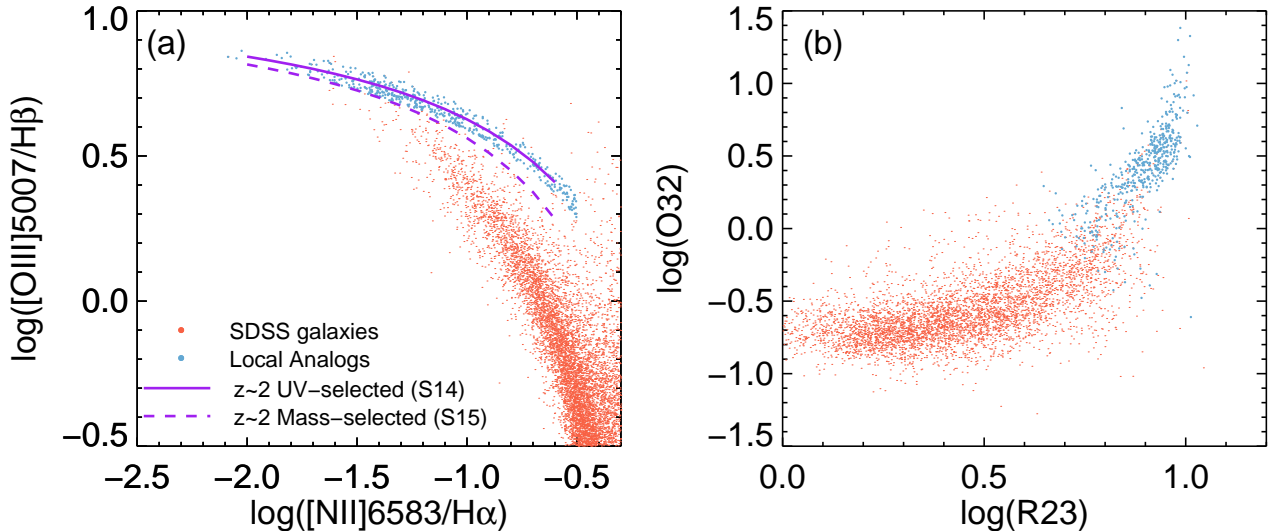


Figure 1. Panel (a): $[\text{O III}]/\text{H}\beta$ versus $[\text{N II}]/\text{H}\alpha$ BPT diagram. The blue points represent the local analogs of high-redshift galaxies selected in this work, and the red points represent the galaxies in the SDSS reference galaxy sample. The purple solid and dashed line represent the $z \sim 2$ BPT locus in UV-selected star-forming galaxies (Steidel et al. 2014, S14) and mass-selected star-forming galaxies (Shapley et al. 2015, S15) at $z \sim 2$, respectively. Panel (b): O32 versus R23 diagram. The blue points represent the local analogs of high-redshift galaxies and the red points represent the galaxies in the SDSS reference galaxy sample.

A total of 458 unique galaxies are selected as local analogs of high-redshift galaxies based on the above selection criteria (blue points in Figure 1(a)).

Figure 1(b) shows the distribution of our analogs on the O32 versus R23 diagnostic diagram. These analogs also share the same region as high-redshift star-forming galaxies on this diagnostic diagram (Nakajima et al. 2013; Nakajima & Ouchi 2014; Ly et al. 2015, 2016; Shapley et al. 2015), implying that these analogs share similar ionization parameters and metallicities with high-redshift star-forming galaxies.

Here, we summarize the properties of the analogs. The median stellar mass of our local analog is $\log(M_*/M_\odot) = 9.0^{+0.6}_{-0.8}$ ². The median SFR and sSFR are $3.5^{+12.0}_{-3.1} M_\odot \text{ yr}^{-1}$ and $6.3^{+15.0}_{-5.7} \text{ Gyr}^{-1}$, respectively. The sSFR of the local analogs is comparable to that in $z \sim 2$ star-forming galaxies with similar stellar mass (e.g., Rodighiero et al. 2011). Furthermore, these analogs closely resemble the ISM conditions in $z \sim 2 - 3$ galaxies (e.g., Nakajima & Ouchi 2014; Sanders et al. 2016), including high ionization parameters ($\log q = 7.9 \pm 0.2 \text{ cm}^{-1}$) and high electron densities ($n_e = 120^{+146}_{-106} \text{ cm}^{-3}$).

The local analog galaxies selected by the above criterion share the same location of the BPT diagram with UV-selected galaxies $z \sim 2$. UV-selected galaxies only

represent about 50% of the full star-forming galaxy census at $z \sim 2$ (e.g., Reddy et al. 2005; Ly et al. 2011; Guo et al. 2012). Shapley et al. (2015) found that the $[\text{O III}]/\text{H}\beta$ ratios in mass-selected star-forming galaxies are lower than those in UV-selected galaxies at $z \sim 2$ (also see Dickey et al. 2016). Therefore, the ISM conditions in our local analogs resemble those in $z \sim 2$ UV-selected galaxies, but may not fully represent the ISM conditions in all $z \sim 2$ star-forming galaxies.

2.2. SDSS Reference Galaxy Sample

We select a sample of galaxies observed in the SDSS from the MPA-JHU value added catalog for SDSS Data Release 7 (DR7, Abazajian et al. 2009). The following criteria are applied: (1) The objects are classified as either star-forming or starburst galaxies in the MPA/JHU catalog, in which the criteria adopted from Kewley et al. (2001) were used to separate star-forming/starburst galaxies from AGNs on the BPT diagram; (2) The S/Ns of $[\text{O II}]\lambda 3727$, $\text{H}\beta$, $[\text{O III}]\lambda\lambda 4959, 5007$, $\text{H}\alpha$ and $[\text{N II}]\lambda 6584$ emission lines are greater than 10; (3) The fiber covering factors³ are greater than 25%. A total of 91,469 SDSS galaxies that meet above criteria are selected. We refer this sample of galaxies as “SDSS reference galaxy sample” in this paper.

In our local analog selections, we apply a $N2 < -0.5$ cut to reduce the contamination of AGN. This selection

² In this paragraph, the uncertainties represent the 16th and 84th percentiles of the distribution of the parameters.

³ The ratio of the fiber flux to the total flux in r band

criterion removes metal-rich galaxies at the high mass end (see details in B16). We further apply the same $N2$ cut to the SDSS galaxy and select a total of 39,875 galaxies. We refer this sample of galaxies as “SDSS reference galaxy sample with $N2 < -0.5$ ”.

3. METALLICITY MEASUREMENTS

We implement the following eight strong line methods to measure the gas-phase oxygen abundance in the local analogs of high-redshift galaxies and SDSS galaxies in the reference sample.

(1) We measure the gas-phase oxygen abundance using the $N2$ - and $O3N2$ -metallicity relations adopted from PP04. PP04 established these empirical relations by combining the direct T_e metallicity and metallicity derived from detailed photoionization modeling at high metallicity end ($12 + \log(O/H) > 8.5$) in a sample of H II regions in nearby galaxies. The $N2$ and $O3N2$ indices have been widely used to measure metallicities in high redshift galaxies (e.g., Erb et al. 2006; Hainline et al. 2009; Bian et al. 2010; Steidel et al. 2014; Sanders et al. 2015), even though it is unclear whether these empirical calibrations are valid for high-redshift metallicity estimation due to the strong evolution of the ISM conditions.

(2) We measure the metallicities and the ionization parameters using the $R23$ and $O32$ indices by adopting the Kobulnicky & Kewley (2004, KK04 hereafter) recipe. KK04 established analytic relations of $R23$, $O32$, the ionization parameter, and the metallicity by fitting the Kewley et al. (2001) photoionization models. These models use the STARBURST99 (Leitherer et al. 1999) stellar population synthesis models to generate the input ionizing radiation field. This information is then inputted into the MAPPINGS III code (Binette et al. 1985; Sutherland & Dopita 1993) to construct photoionization models over a wide range of the metallicities and the ionization parameters. We use the $N2O2$ to determine whether each galaxy locates on the upper or lower $R23$ branch and compute the metallicity and the ionization parameter iteratively until the metallicity converge. We refer readers to section A2.3 in Kewley & Ellison (2008) for more detail.

(3) We compute the metallicities and the ionization parameters simultaneously by fitting multiple diagnostic lines with photoionization models using the IZI program (Inferring metallicities (Z) and Ionization parameters, Blanc et al. 2015). This program uses Bayesian inference to compute the joint and marginalized probability density functions of the metallicity and the ionization parameter for a set of emission line flux measurements based on photoionization models. We use a set of metallicity and ionization parameter sensitive emission lines, including $[O II]\lambda 3727$, $H\beta$, $[O III]\lambda 4959, 5007$, $H\alpha$,

$[N II]\lambda 6584$, and $[S II]\lambda \lambda 6717, 6731$ for the fitting and adopt the Kewley et al. (2001) photoionization models.

(4) We measure the metallicities using the new metallicity calibrations proposed by Dopita et al. (2016, D16 hereafter). This new calibration is based on a new grid of photoionization models from the photoionization code MAPPINGS VI (Sutherland et al. 2015 in prep.). D16 found that the combination of $[N II]\lambda 6584/[S II]\lambda \lambda 6717, 6731$ and $[N II]\lambda 6584/H\alpha$ provides a good metallicity diagnostics, which is not sensitive to ionization parameters and electron densities. Furthermore, these lines are close together in wavelength, so they are less affected by reddening and can be easily observed simultaneously in high-redshift galaxies.

(5) We adopt the metallicities in the MPA/JHU catalog from Tremonti et al. (2004, T04 hereafter). The metallicity for each galaxy is estimate by fitting the Charlot & Longhetti (2001) models to strong emission lines, including $[O II]\lambda 3727$, $H\beta$, $[O III]\lambda \lambda 4959, 5007$, $H\alpha$, $[N II]\lambda 6584$, and $[S II]\lambda \lambda 6717, 6731$. The Charlot & Longhetti (2001) models use the Bruzual & Charlot (2003) stellar synthesis models to characterize the ionizing radiation field and the photoionization code CLOUDY (Ferland et al. 1998) is applied to compute the emission line ratios.

(6) We compute the metallicity using the HII-CHI-mistry (HCm, Pérez-Montero 2014). This code fits a large grids of photoionization models to the emission line ratios of $[O II]\lambda 3727/H\beta$, $[O III]\lambda 5007/H\beta$, $[N II]\lambda 6584/H\beta$, and $[S II]\lambda \lambda 6717, 6731/H\beta$. The photoionization models are computed using the photoionization code CLOUDY (Ferland et al. 2013) and the ionizing radiation field generated from the POPSTAR (Mollá et al. 2009).

(7) We compute the metallicity using the $R23$ and $O32$ indices from McGaugh (1991, M91 hereafter). The M91 calibration is based on the detailed H II region models using the photoionization code CLOUDY (Ferland et al. 1998) and the Mihalas (1972) stellar atmosphere models.

The methods (2)-(7) are all based on photoionization models codes, either MAPPINGS or CLOUDY. These methods either solve the relations between the metallicity and a set of emission line ratios (e.g., $R23$, $O32$) analytically (e.g., KK04, D16, M91) or derive the metallicity by fitting a full set of emission-line relative flux to photoionization grids (e.g., IZI, T04, HCm).

4. MASS-METALLICITY RELATION

We compare the mass-metallicity relations of the SDSS galaxies in the reference sample and our local analogs of high-redshift galaxies for each metallicity calibration. Figure 2 shows the evolution of mass-metallicity relations between the SDSS reference galaxies (red lines) and our local analogs (blue circles). We

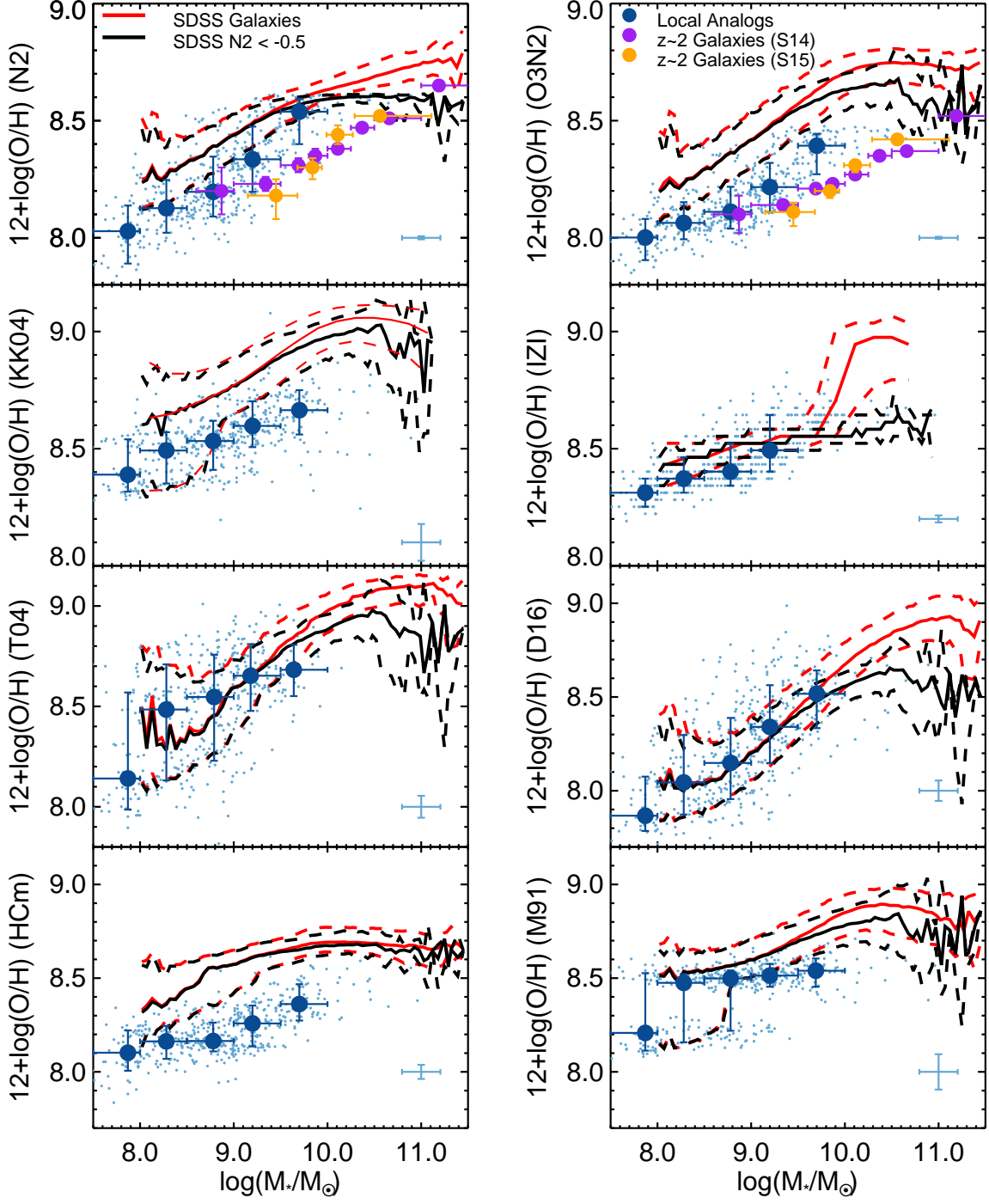


Figure 2. Mass-metallicity relation of SDSS galaxies and the local analogs of high-redshift galaxies. The metallicities are estimated based on N2 and O3N2 indicators by Pettini & Pagel (2004), R23 and O32 indicators by Kobulnicky & Kewley (2004, KK04) and McGaugh (1991, M91), combination of N2 and N2S2 indicators by Dopita et al. (2016, D16), and fitting photoionization models with all the available diagnostic lines simultaneously by IZI code (Blanc et al. 2015), Tremonti et al. (2004, T04), and HCm code (Pérez-Montero 2014). The light blue points represent the mass-metallicity relation of individual local analogs, and the dark blue points with error bars represent the median metallicity of local analogs in each stellar mass bin. The horizontal error bar shows the stellar mass range in each mass bin, and the vertical error bar represents the 16th and 84th percentiles of the oxygen abundance distribution in each mass bin. The red solid line represents the median mass-metallicity relation of SDSS galaxies, and two dashed lines represent the 16th and 84th percentiles of the oxygen abundance distribution. The black solid curves represent the SDSS galaxies with $N2 < -0.5$ cuts as we applied for our local analog selection. The error bar at the right bottom corner of each of the plot represents a typical uncertainty of metallicity and stellar mass estimation for an individual local analog galaxy. The purple points and orange triangles with error bars represent the mass-metallicity relation of $z \sim 2$ star-forming galaxies from Steidel et al. (2014, S14) and Sanders et al. (2015, S15), respectively. The horizontal error bar shows the stellar mass range in each mass bin, and the vertical error bar indicates the uncertainty in oxygen abundance estimated from the uncertainty on composite emission-line fluxes for each stellar mass bin.

quantify the evolution by computing the metallicity difference between the SDSS galaxies and the local analogs ($\Delta Z = Z(\text{SDSS}) - Z(\text{analog})$) for a given galaxy stellar mass bin.

We carefully select the appropriate mass bin to use for the metallicity comparison. First, we choose a mass bin that is not affected by the selection effect on the $N2 < -0.5$ cut. We compare the mass-metallicity relation in the SDSS main galaxy sample and SDSS galaxy sample with $N2 < -0.5$ and find that the two mass-metallicity relations are consistent with each other at the low mass end and start to show discrepancies at $\log(M_*/M_\odot) > 9.5$ in all eight diagnostic methods (red and black dashed lines in Figure 2). Therefore, the selection effect ($N2 < -0.5$) does not affect the mass-metallicity relation at $\log(M_*/M_\odot) < 9.5$. Secondly, we would like to choose the mass bin whose median metallicity of the local analogs are comparable to that in $z \sim 2-3$ galaxies (Figure 2). We choose the mass bin of $8.5 < \log(M_*/M_\odot) < 9.0$ to compare the ΔZ between local analogs and SDSS galaxies to meet the above two requirements.

Table 1 summarizes the metallicity differences between the SDSS galaxies and the local analogs (ΔZ) in the mass bin of $8.5 < \log(M_*/M_\odot) < 9.0$ based on the eight metallicity estimation methods in Figure 2. There exist significant metallicity differences between the SDSS galaxies and the local analogs in all eight metallicity estimation methods. The ΔZ changes from -0.09 dex to 0.39 dex depending on the method used.

The ΔZ results derived from the two empirical calibrations ($N2$ and $O3N2$) are not consistent with each other. $\Delta Z(O3N2)$ is larger than $\Delta Z(N2)$ by about 0.05 dex. This discrepancy was also found in high-redshift mass-metallicity relation studies (e.g., Steidel et al. 2014; Zahid et al. 2014b; Sanders et al. 2015). This discrepancy is primarily caused by the offset between the local galaxies and high-redshift galaxies on the $[O\text{ III}]\lambda 5007/H\beta$ versus $[N\text{ II}]\lambda 6584/H\alpha$ BPT diagram. This offset could be due to higher electron densities and ionization parameters, harder ionization radiation fields, various N/O ratios, AGN/shock contributions, and/or selection effects (e.g., Liu et al. 2008; Brinchmann et al. 2008; Kewley et al. 2013a,b; Juneau et al. 2014; Masters et al. 2014, 2016; Newman et al. 2014; Steidel et al. 2014; Shapley et al. 2015; Bian et al. 2016).

The ΔZ results derived from the photoionization model grids are different. The KK04, IZI and D16 calibrations are all based on the MAPPINGS photoionization models, however, the ΔZ s from these three methods vary from -0.03 to 0.19 . The D16 and IZI methods yield a much smaller ΔZ than the KK04 calibration (Table 1). The major cause of this discrepancy is that the

R23 methods have a fixed metallicity (e.g., O2N2 value) threshold to break the lower and upper R23 branch degeneracy. However, the R23 metallicity upper/lower branch turnover points decrease with the increasing ionization parameters in photoionization models (e.g., Figure 7 in Kobulnicky & Kewley 2004). This metallicity threshold is chosen to meet the conditions of low ionization parameter in local star-forming galaxies. However, this threshold tends to place galaxies with high ionization parameters on the upper R23 branch onto the lower R23 branch, which underestimates the metallicity in our analog galaxies and overestimates the ΔZ . On the other hand, the IZI method considers all the available emission line information, providing a more robust metallicity estimation based on the photoionization models.

The ionizing radiation field also makes significant impact on the ΔZ results based on the photoionization models. For example, both T04 and HcM methods fit a full set of emission-line relative fluxes to the photoionization models from CLOUDY code, however, the ΔZ s show ~ 0.4 dex difference. One of the major differences of these two photoionization models is that the input ionizing radiation field, that T04 and HcM implement the BC03 and POPSTAR stellar synthesis models, respectively. The BC03 model yields harder UV spectra than the POPSTAR model (Mollá et al. 2009).

5. DISCUSSION

5.1. Effects of Shocks and AGNs

Shocks and/or AGNs in galaxies could enhance the $[N\text{ II}]\lambda 6584$ flux, resulting in an overestimation of the $N2$ -based metallicity for galaxies, in particular in high-redshift galaxies (e.g., Newman et al. 2013; Maier et al. 2014). The local analogs allow us to access the diagnostic lines that are sensitive to the shocks and/or AGNs, including the $[S\text{ II}]\lambda\lambda 6717, 6731$, $[O\text{ I}]\lambda 6300$ emission lines. These lines are sensitive to the hardness of the ionizing radiation field. We use the $[O\text{ III}]/H\beta$ versus $[S\text{ II}]/H\alpha$ and $[O\text{ I}]/H\alpha$ BPT diagnostic diagrams (S2 and O1 BPT diagrams) to remove the local analogs whose $[N\text{ II}]\lambda 6584$ emission line flux could be potentially contaminated by AGN/shock excitation.

Figure 3 shows the S2 and O1 BPT diagnostic diagrams. The solid lines are adopted from Kewley et al. (2006) to separate the pure star forming galaxies and galaxies with AGNs/strong shocks. We offset the Kewley et al. (2006) criteria by $+0.05$ dex in the $[O\text{ III}]/H\beta$ direction to meet the conditions in high-redshift galaxies. In the BPT diagrams, we are able to identify galaxies that are potentially contaminated by AGNs/strong shocks (red squares in Figure 3). We establish a new clean sample of the local analogs of high-redshift galaxies by removing galaxies ($\sim 20\%$ of

Table 1. The metallicity difference between SDSS galaxies and local analogs of high-redshift galaxies in $8.5 < \log(M_*/M_\odot) < 9.0$ mass bin

Method	N2	O3N2	KK04	IZI	T04	D16	HCm	M91
ΔZ ^a	$0.19^{+0.11}_{-0.15}$ ^b	$0.25^{+0.07}_{-0.11}$	$0.19^{+0.12}_{-0.08}$	$0.12^{+0.06}_{-0.12}$	$-0.09^{+0.32}_{-0.21}$	$-0.03^{+0.19}_{-0.24}$	$0.39^{+0.06}_{-0.10}$	$0.07^{+0.28}_{-0.04}$
ΔZ ^c	$0.18^{+0.11}_{-0.14}$	$0.24^{+0.07}_{-0.11}$	0.18 ± 0.07	$0.12^{+0.06}_{-0.12}$	$-0.12^{+0.28}_{-0.19}$	$-0.07^{+0.09}_{-0.19}$	$0.40^{+0.04}_{-0.10}$	$0.06^{+0.05}_{-0.04}$

^aThe first row: the metallicity difference between the SDSS galaxies in the reference sample and the full sample of local analogs.

^bThe errors represent the 16th and 84th percentiles of the ΔZ distribution.

^cThe second row: the metallicity difference between the SDSS galaxies in the reference sample and local analogs without potential AGN/shock contamination.

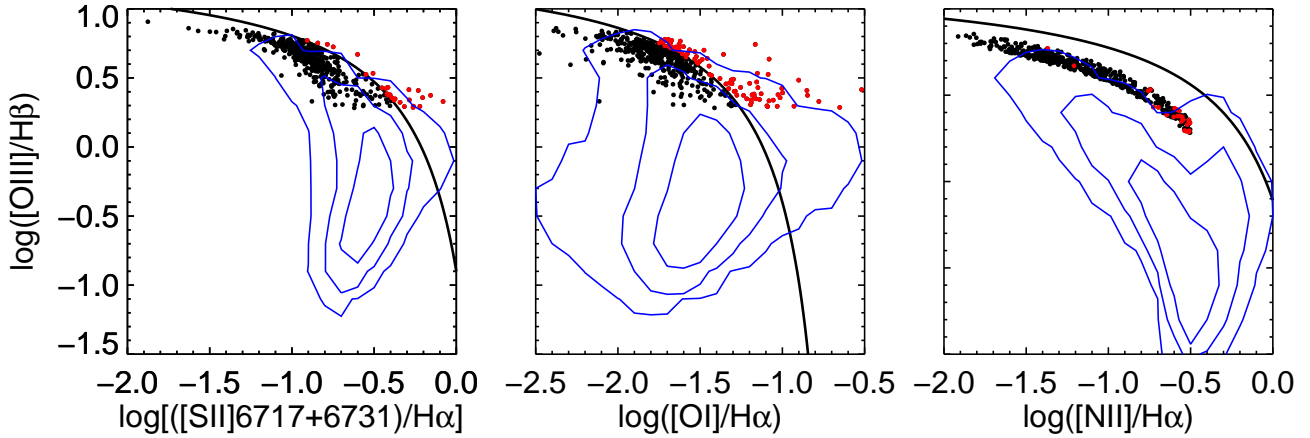


Figure 3. S2, O1, and N2 BPT diagrams. The blue contours represent 1σ , 2σ , and 3σ distributions of the SDSS reference galaxy sample in the BPT diagrams. The black solid line is the separation of star-forming region and AGN/shock region in the BPT diagram (Kewley et al. 2006). The red filled circles represent the local analog galaxies with potential AGN/shock contamination, and the black circles represent the local analog galaxies with pure star formation.

the total sample of the local analogs) located in the AGN/shocks regions either in the S2 or O1 BPT diagram. The $[\text{N II}]/\text{H}\alpha$ in this new sample of local analogs is less affected by AGNs and/or strong shocks. We thus expect that the $N2$ -based metallicity is more reliable in this new clean sample. Figure 4 shows the mass-metallicity relation in the new clean sample of local analogs of high-redshift galaxies, and we also summarize the new ΔZ results estimated from the eight methods in the second row of Table 1. We find that mass-metallicity relation in this new sample of the local analogs is consistent with that in the original sample of local analogs. It suggests that shocks/AGNs do not significantly affect the $N2$ -based metallicity estimation in the local analogs of high-redshift galaxies. The local analogs assemble similar physical properties to high-redshift star-forming galaxies (B16). We thus expect the effects of AGN/strong shocks would be negligible for the global metallicity measurement of high-redshift galaxies, in particular at the low mass end ($\log(M_*/M_\odot) < 9.5$).

5.2. Applicability of the Photoionization Models

The metallicity estimation based on photoionization models relies on the accuracy of the photoionization models. The systematic uncertainties in photoionization models could affect the metallicity estimation in galaxies (e.g., Kewley & Dopita 2002; Blanc et al. 2015). The two major uncertainties are the input ionizing radiation field based on the stellar synthesis models and the star formation history, and the relation between N/O and oxygen abundance (O/H).

The harder ionizing radiation field provides more high energy ionizing photons, which enhance the fluxes of the $[\text{N II}]\lambda 6584$ and $[\text{O III}]\lambda 5007$ emission line. Therefore, the harder radiation field increases the $N2$, $O3N2$, $R23$ indices for a given metallicity, affecting the metallicity estimation based on the above metallicity diagnostic indices. Steidel et al. (2014) proposed that high-redshift galaxies have a harder radiation field due to the stellar binarity and rotation (e.g., Eldridge & Stanway 2009; Levesque et al. 2010; Steidel et al. 2016). This requires the application of the photoionization models with different ionizing radiation field to low- and high-redshift

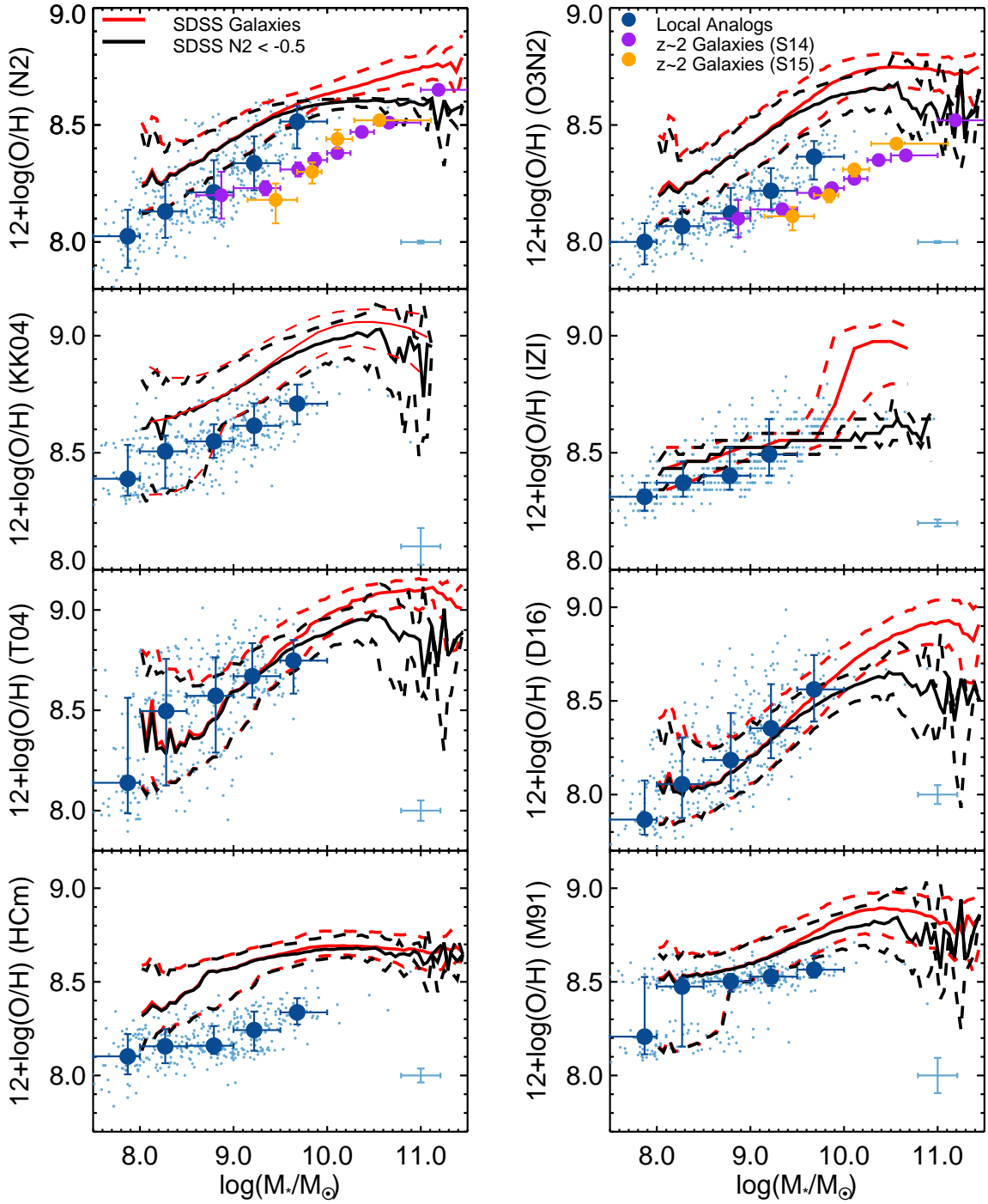


Figure 4. Similar to Figure 1, but we exclude local analog galaxies that are potentially affected by AGNs and/or shocks based on the S2 and O1 BPT diagrams. AGN/shock contamination does not have a significant impact on the mass-metallicity relation.

galaxies.

The $N2$ and $O3N2$ indices are also sensitive to nitrogen abundance, so the relation between N/O and oxygen abundance is crucial for obtaining a reliable oxygen abundance measurements. An evolution in the N/O versus O/H relation with redshift (e.g., Masters et al. 2014, 2016; Shapley et al. 2015) would affect the metallicity estimates based on the $N2$ and $O3N2$ indices (c.f. Dopita et al. 2016; Strom et al. 2016). This evolution does not affect the $R23$ index, but it can cause issues when using the $N2O2$ index to determine whether one galaxy is located in the upper or lower $R23$ branch.

However, we have very limited information on how the radiation field and N/O evolve with redshift to provide reliable inputs for the photoionization models. Further detailed studies on either deep spectra of the individual analog galaxies or composite spectra of a sample of local analogs would provide us better constraints on the evolution of radiation field and N/O ratio (Bian et al. in prep).

6. CONCLUSIONS

We investigate the mass-metallicity relation in the local analogs of high-redshift galaxies. These local analogs have similar interstellar medium (ISM) conditions to high-redshift galaxies, which provide a great opportunity to understand how the ISM conditions affect the metallicity measurements in high-redshift galaxies. We summarize our main results as follows:

- The well-detected full set of rest-frame optical diagnostic lines allow us to study the mass-

metallicity relation in the local analogs and normal SDSS galaxies in the reference sample using eight different metallicity diagnostics, including both empirical calibrations and metallicity diagnostics based on photoionization models.

- The metallicity difference between the local analogs and normal SDSS galaxies in the mass bin of $8.5 < \log(M_*/M_\odot) < 9.0$ varies between -0.09 and 0.39 dex depending on the strong-line metallicity diagnostic method used.
- We remove the local analogs whose emission lines are potentially contaminated by AGN/shock excitation using the [O III]/H β versus [S II]/H α and [O I]/H α BPT diagnostic diagrams. The mass-metallicity relation does not change after we remove the local analogs with AGN/shocks contamination, suggesting that the AGN/shock contribution in our local analogs is negligible for the global metallicity estimation in our local analogs.

We are very grateful to the anonymous referee for comments and suggests to improve the manuscript. M.D. and L.K. acknowledge the support of the Australian Research Council (ARC) through Discovery project DP130103925. M.D. would also like to thank the Dean-ship of Scientific Research (DSR), King AbdulAziz University for additional financial support as Distinguished Visiting Professor under the KAU Hi-Ci program. G.B. is supported by CONICYT/FONDECYT, Programa de Iniciacion, Folio 11150220.

Facility: SDSS

REFERENCES

- Abazajian, K. N., Adelman-McCarthy, J. K., Agüeros, M. A., et al. 2009, *ApJS*, 182, 543
- Andrews, B. H., & Martini, P. 2013, *ApJ*, 765, 140
- Baldwin, J. A., Phillips, M. M., & Terlevich, R. 1981, *PASP*, 93, 5
- Bian, F., Kewley, L. J., Dopita, M. A., & Juneau, S. 2016, *ApJ*, 822, 62
- Bian, F., Fan, X., Bechtold, J., et al. 2010, *ApJ*, 725, 1877
- Binette, L., Dopita, M. A., & Tuohy, I. R. 1985, *ApJ*, 297, 476
- Blanc, G. A., Kewley, L., Vogt, F. P. A., & Dopita, M. A. 2015, *ApJ*, 798, 99
- Brinchmann, J., Pettini, M., & Charlot, S. 2008, *MNRAS*, 385, 769
- Bruzual, G., & Charlot, S. 2003, *MNRAS*, 344, 1000
- Cardelli, J. A., Clayton, G. C., & Mathis, J. S. 1989, *ApJ*, 345, 245
- Charlot, S., & Longhetti, M. 2001, *MNRAS*, 323, 887
- Davé, R., Finlator, K., & Oppenheimer, B. D. 2012, *MNRAS*, 421, 98
- Dickey, C. M., van Dokkum, P. G., Oesch, P. A., et al. 2016, *ApJL*, 828, L11
- Dopita, M. A., Kewley, L. J., Sutherland, R. S., & Nicholls, D. C. 2016, *Ap&SS*, 361, 61
- Eldridge, J. J., & Stanway, E. R. 2009, *MNRAS*, 400, 1019
- Erb, D. K., Shapley, A. E., Pettini, M., et al. 2006, *ApJ*, 644, 813
- Ferland, G. J., Korista, K. T., Verner, D. A., et al. 1998, *PASP*, 110, 761
- Ferland, G. J., Porter, R. L., van Hoof, P. A. M., et al. 2013, *RMxAA*, 49, 137
- Finlator, K., & Davé, R. 2008, *MNRAS*, 385, 2181
- González Delgado, R. M., Cid Fernandes, R., García-Benito, R., et al. 2014, *ApJL*, 791, L16
- Guo, Y., Gialavalisco, M., Cassata, P., et al. 2012, *ApJ*, 749, 149
- Guo, Y., Koo, D. C., Lu, Y., et al. 2016, *ApJ*, 822, 103
- Hainline, K. N., Shapley, A. E., Kornei, K. A., et al. 2009, *ApJ*, 701, 52
- Juneau, S., Bournaud, F., Charlot, S., et al. 2014, *ApJ*, 788, 88
- Kewley, L. J., & Dopita, M. A. 2002, *ApJS*, 142, 35
- Kewley, L. J., Dopita, M. A., Leitherer, C., et al. 2013a, *ApJ*, 774, 100
- Kewley, L. J., Dopita, M. A., Sutherland, R. S., Heisler, C. A., & Trevena, J. 2001, *ApJ*, 556, 121
- Kewley, L. J., & Ellison, S. L. 2008, *ApJ*, 681, 1183
- Kewley, L. J., Groves, B., Kauffmann, G., & Heckman, T. 2006, *MNRAS*, 372, 961
- Kewley, L. J., Maier, C., Yabe, K., et al. 2013b, *ApJL*, 774, L10
- Kewley, L. J., Zahid, H. J., Geller, M. J., et al. 2015, *ApJL*, 812, L20

- Kewley, L. J., Yuan, T., Nanayakkara, T., et al. 2016, *ApJ*, 819, 100
- Kobulnicky, H. A., & Kewley, L. J. 2004, *ApJ*, 617, 240
- Leitherer, C., Schaerer, D., Goldader, J. D., et al. 1999, *ApJS*, 123, 3
- Levesque, E. M., Kewley, L. J., & Larson, K. L. 2010, *AJ*, 139, 712
- Lilly, S. J., Carollo, C. M., Pipino, A., Renzini, A., & Peng, Y. 2013, *ApJ*, 772, 119
- Liu, X., Shapley, A. E., Coil, A. L., Brinchmann, J., & Ma, C.-P. 2008, *ApJ*, 678, 758
- Lu, Y., Blanc, G. A., & Benson, A. 2015, *ApJ*, 808, 129
- Ly, C., Malkan, M. A., Hayashi, M., et al. 2011, *ApJ*, 735, 91
- Ly, C., Malkan, M. A., Nagao, T., et al. 2014, *ApJ*, 780, 122
- Ly, C., Malkan, M. A., Rigby, J. R., & Nagao, T. 2016, *ApJ*, 828, 67
- Ly, C., Rigby, J. R., Cooper, M., & Yan, R. 2015, *ApJ*, 805, 45
- Ma, X., Hopkins, P. F., Faucher-Giguère, C.-A., et al. 2016, *MNRAS*, 456, 2140
- Maier, C., Lilly, S. J., Ziegler, B. L., et al. 2014, *ApJ*, 792, 3
- Maiolino, R., Nagao, T., Grazian, A., et al. 2008, *A&A*, 488, 463
- Masters, D., Faisst, A., & Capak, P. 2016, *ApJ*, 828, 18
- Masters, D., McCarthy, P., Siana, B., et al. 2014, *ApJ*, 785, 153
- McGaugh, S. S. 1991, *ApJ*, 380, 140
- Mihalas, D. 1972, Non-LTE model atmospheres for B and O stars.
- Mollá, M., García-Vargas, M. L., & Bressan, A. 2009, *MNRAS*, 398, 451
- Nakajima, K., & Ouchi, M. 2014, *MNRAS*, 442, 900
- Nakajima, K., Ouchi, M., Shimasaku, K., et al. 2013, *ApJ*, 769, 3
- Newman, S. F., Genzel, R., Förster Schreiber, N. M., et al. 2013, *ApJ*, 767, 104
- Newman, S. F., Buschkamp, P., Genzel, R., et al. 2014, *ApJ*, 781, 21
- Osterbrock, D. E., & Ferland, G. J. 2006, *Astrophysics of gaseous nebulae and active galactic nuclei*
- Pérez-Montero, E. 2014, *MNRAS*, 441, 2663
- Pettini, M., & Pagel, B. E. J. 2004, *MNRAS*, 348, L59
- Reddy, N. A., Erb, D. K., Steidel, C. C., et al. 2005, *ApJ*, 633, 748
- Rodighiero, G., Daddi, E., Baronchelli, I., et al. 2011, *ApJL*, 739, L40
- Salim, S., Lee, J. C., Davé, R., & Dickinson, M. 2015, *ApJ*, 808, 25
- Sanders, R. L., Shapley, A. E., Kriek, M., et al. 2015, *ApJ*, 799, 138
- . 2016, *ApJ*, 816, 23
- Savaglio, S., Glazebrook, K., Le Borgne, D., et al. 2005, *ApJ*, 635, 260
- Shapley, A. E., Reddy, N. A., Kriek, M., et al. 2015, *ApJ*, 801, 88
- Shirazi, M., Brinchmann, J., & Rahmati, A. 2014, *ApJ*, 787, 120
- Steidel, C. C., Strom, A. L., Pettini, M., et al. 2016, *ApJ*, 826, 159
- Steidel, C. C., Rudie, G. C., Strom, A. L., et al. 2014, *ApJ*, 795, 165
- Strom, A. L., Steidel, C. C., Rudie, G. C., et al. 2016, *ArXiv e-prints*, arXiv:1608.02587
- Sutherland, R. S., & Dopita, M. A. 1993, *ApJS*, 88, 253
- Tremonti, C. A., Heckman, T. M., Kauffmann, G., et al. 2004, *ApJ*, 613, 898
- Zahid, H. J., Dima, G. I., Kudritzki, R.-P., et al. 2014a, *ApJ*, 791, 130
- Zahid, H. J., Geller, M. J., Kewley, L. J., et al. 2013, *ApJL*, 771, L19
- Zahid, H. J., Kashino, D., Silverman, J. D., et al. 2014b, *ApJ*, 792, 75